Medical Physics
The International Journal of Medical Physics Research and Practice

MR image artifacts from periodic motion

Michael L. Wood and R. Mark Henkelman

Citation: Medical Physics **12**, 143 (1985); doi: 10.1118/1.595782
View online: http://dx.doi.org/10.1118/1.595782
View Table of Contents: http://scitation.aip.org/content/aapm/journal/medphys/12/2?ver=pdfcov
Published by the American Association of Physicists in Medicine

MR image artifacts from periodic motion

Michael L. Wood and R. Mark Henkelman
Ontario Cancer Institute and Department of Medical Biophysics, University of Toronto, 500 Sherbourne Street, Toronto, Canada M4X 1K9

(Received 5 January 1984; accepted for publication 13 August 1984)

Artifacts due to periodic motion during the acquisition of magnetic resonance (MR) images have been studied. A mechanical device was constructed to oscillate a small sample along any line within a 0.15-T Technicare imager. Two- and three-dimensional images were obtained using various frequencies and amplitudes of oscillation. Computer simulations of these experiments yielded images which agreed with the experiments. We demonstrated that movement influences MR images locally through blurring, and also generates ghost artifacts along the phase-encoding directions of the Fourier transform imaging technique.

Key words: MR imaging, artifacts

I. INTRODUCTION

Data acquisition in magnetic resonance (MR) imaging requires from 2 to 30 min, during which appreciable physiological movement occurs. Figure 1 demonstrates how breathing affects MR images. This transverse section through the liver exhibits dark and bright bands, which interfere with anatomical detail. In this case, the most intense bands are artifactual ghost images of the anterior surface. Clearly, the clinical interpretation of MR images of the abdomen depends on understanding, and eventually correcting or eliminating, these motion artifacts.

Rather than attempt a direct analysis of artifacts in clinical images, we have studied a much simpler problem—the point spread function (PSF) of a pointlike object in simple harmonic motion. To first order, MR imaging can be considered a linear system. Specific sources of nonlinearities include noise, nonideal magnetic field gradients, and nonuniform tip angles. To the extent that nonlinearities can be neglected, an MR image can be considered the convolution of the object with the point spread function.

Much motion in the body is approximately periodic. Quiet breathing, for example, displaces the thoracic wall and abdominal contents by 1–2 cm, approximately every 5 s.[1] Movement associated with the cardiac cycle exhibits higher frequencies, typically around 1 Hz. This paper demonstrates that simple harmonic motion leads to artifacts, or "ghosts," repeated at constant spacings. Figure 1 provides evidence that complicated images, too, exhibit this feature.

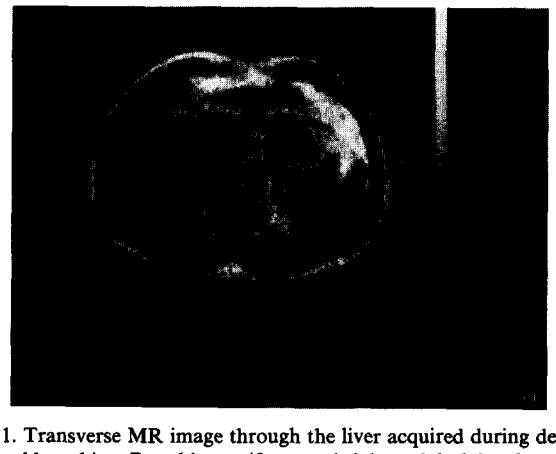

FIG. 1. Transverse MR image through the liver acquired during deep abdominal breathing. Breathing artifacts are bright and dark bands repeated vertically across the image. The additional vertical column of artifact on the right-hand side of the image is caused by movement within the stomach.

The first step in the analysis determines the two-dimensional MR image of a pointlike object at rest. Next, the point spread function is derived for a point following simple harmonic motion along the x direction, which is defined in Fig. 2. Similarities allow a condensed treatment for motion in the y and z directions, as well as motion in three-dimensional imaging. Computer simulations facilitate numerical evaluation of the mathematics. Simulated images from a variety of motions are finally compared with experimental images obtained with the same periodic motion.

II. METHOD

MR images of a point were simulated in FORTRAN. Programs considered all stages of data acquisition and reconstruction of a point magnetization, including selective excitation, echo formation, discrete sampling, and relaxation processes, but did not model noise, magnetic field inhomogeneities, or temporal instabilities in the imaging system. Simulated data could be reconstructed and analyzed directly on the MR imager.

Experimental images were acquired on a Teslacon 0.15-T MR imager. A mechanical device was designed and constructed to displace periodically a small object along any line

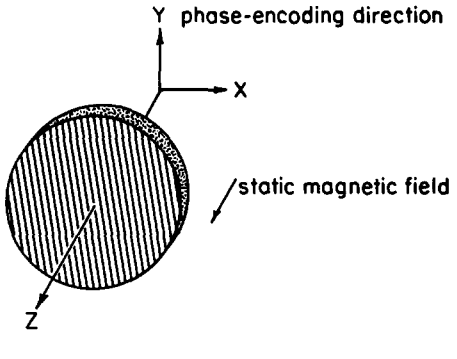

FIG. 2. Coordinate system for MR imaging.

 0094-2405/85/020143-09$01.20

within the imaging volume. The driving mechanism was located 3 m from the imager to avoid interference from ferromagnetic materials. Motion amplitude, frequency, and phase were varied to model organ motion. A solenoidal coil, which moved with the sample, was fabricated for these experiments. There were seven windings of ten turns each over a glass tube of 1.5-mm inner diameter. The outer diameter of the coil was 13 mm and the length was 6 mm. The signal-to-noise was the maximum voltage of a signal with a sample present, divided by the root-mean-squared deviation of the voltage with a sample absent. With this coil, the signal-to-noise per unit volume was 500 cm^{-3}, which was a factor of 200 improvement over the 28-cm-diam head coil supplied with the imager. Vacuum grease was chosen for the sample because of its rapid signal decay (at 6.25 MHz, $T_1 = 0.36$ s and $T_2 = 0.14$ s), and also the ease with which it could be handled. The sample used to simulate a point object was cylindrical, with diameter 1.5 mm and height 3 mm. These dimensions compare to a typical $1.1 \times 2.1 \times 10$ mm voxel.

III. RESULTS AND DISCUSSION

A. Two-dimensional MR images

1. No motion

The principles of magnetic resonance imaging and the implementation of various imaging techniques have been described.[2–6] Two-dimensional MR Fourier imaging, proposed by Kumar, Welti, and Ernst,[5] is finding the most widespread application. One improvement, first advanced by Edelstein *et al.*,[7] is to modulate the amplitude instead of the duration of the phase-encoding gradient, making the method less sensitive to magnetic field nonuniformities. The steps to acquire a signal, which is one phase-encoded projection, are shown in Fig. 3. After a delay of T_R, the procedure must be repeated N_y times with different phase-encoding gradients to complete the data acquisition for an image. Furthermore, G_y is incremented monotonically in steps of ΔG, from $-[(N_y/2)-1]\Delta G$ to $(N_y/2)\Delta G$. Practical implementations usually employ signal averaging with different combinations of phase shifts of the excitation pulses to suppress zero offsets and to cancel the free-induction decay following the $\pi/2$ pulse. For ease of presentation, the analytical derivations assume only one signal for each phase-encoding gradient. This discrepancy will be considered further when the theory is compared with experimental images.

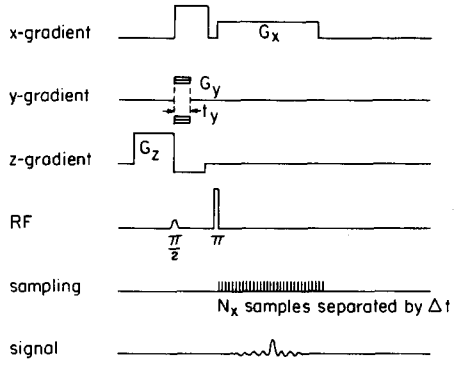

FIG. 3. Pulse timing diagram for a signal in two-dimensional imaging.

To acquire one phase-encoded projection, first, a selective radio-frequency (rf) pulse flips the magnetization vector by $\pi/2$ radians onto the y axis of a reference frame rotating about z at the Larmor frequency. Combining a narrow frequency band rf pulse simultaneously with a magnetic field gradient along the z axis restricts this excitation to a narrow slice in the z direction. Immediately following selective excitation, the transverse component M of a magnetization M_0 at position z is arbitrarily chosen to follow the Gaussian distribution of Eq. (1),

$$M(z) = M_0 \exp[(-1/2)(\sigma\gamma G_z z)^2] , \tag{1}$$

where σ, in combination with the selection gradient G_z, defines the slice thickness, and γ is the gyromagnetic ratio. It will be noted later that the particular form of Eq. (1) influences only the artifact from motion perpendicular to the slice.

A rephasing z gradient realigns the transverse magnetization along a single axis. Immediately following the $\pi/2$ pulse, a y gradient is switched on for a time t_y, during which the Larmor frequency depends on the y coordinate within the selected slice. Upon return to a uniform magnetic field, the Larmor frequency loses its spatial dependence, but the phase of the transverse magnetization now depends on its y position.

A magnetization, which is represented by a delta function at position (x,y), emits an oscillatory signal whose amplitude is, in general, shaped by an apodizing function $E_x(t)$. The signal, which is an echo caused by the nonselective π pulse, is discretely sampled N_x times at intervals of Δt. The x gradient, which exists immediately after the $\pi/2$ pulse, is adjusted so that the echo peaks at the central data sample. Data sample $N_x/2$ also coincides with the time origin for the mathematical development. The phase ϕ of the signal is then given by Eq. (2),

$$\phi(t,G_y) = \gamma(G_x\, xt - G_y\, yt_y) . \tag{2}$$

Magnetic field gradients G_x and G_y encode spatial information into the signal. The sign of the G_y term is negative because the phase-encoding gradient is applied before the echo-forming pulse inverts the phase. The signal is detected in quadrature at a reference frequency equal to the Larmor frequency. The complete set of data $s(t,G_y)$ is composed of N_y complex signals collected under different amounts of phase encoding and apodization in the G_y direction, which is determined by $E_y(G_y)$;

$$s(t,G_y) = \{M_0 E_x(t) E_y(G_y) \exp[i\phi(t,G_y)]\, d(t)\, d(G_y)\} \ast_t \mathrm{III}\left(\frac{t}{N_x \Delta t}\right) \ast_{G_y} \mathrm{III}\left(\frac{G_y}{N_y \Delta G}\right), \tag{3}$$

where

$$d(t) = \mathrm{III}\left(\frac{t}{\Delta t}\right) \Pi\left(\frac{t}{N_x \Delta t}\right), \tag{4}$$

and

$$d(G_y) = \mathrm{III}\left(\frac{G_y}{\Delta G}\right) \Pi\left(\frac{G_y}{N_y \Delta G}\right). \tag{5}$$

In Eq. (3), M_0 is the transverse magnetization from a mag-

netization at $z=0$. For simplicity, complete relaxation between sets of projection measurements is assumed, and no term representing partial recovery is included. Equation (4) accounts for sampling of the time variable. The first component is Bracewell's sampling symbol,[8] $\mathrm{III}(t/\Delta t)$, which is an infinite sequence of delta functions separated by Δt. Multiplication of a function by $\mathrm{III}(t/\Delta t)$ is equivalent to sampling it at intervals of Δt,

$$\mathrm{III}\left(\frac{t}{\Delta t}\right)=\Delta t\sum_{k=-\infty}^{\infty}\delta(t-k\,\Delta t)\,. \tag{6}$$

The N_x temporal samples which compose each phase-encoded projection are selected by multiplying Eq. (6) by the rectangle function[9] $\Pi[t/(N_x\,\Delta t)]$,

$$\Pi[t/(N_x\,\Delta t)]=\begin{cases}0 & t\leqslant(-N_x/2)\Delta t\,,\\ 1 & (-N_x/2)\Delta t<t\leqslant(N_x/2)\Delta t\,,\\ 0 & (N_x/2)\Delta t<t\,.\end{cases} \tag{7}$$

Convolution is denoted by $*$ and the domain is indicated by the subscript. The periodicity introduced by convolution in Eq. (3) makes the frequency domain also discrete.

Kumar, Welti, and Ernst[5] demonstrated that the two-dimensional Fourier transform of the data set described in Eq. (3) represents the physical object convolved with several broader distributions. Since the Fourier kernel is separable, Eq. (8) arises as the product of two one-dimensional Fourier transforms applied to the variables t and G_y in Eq. (3).

$$\begin{aligned}\mathcal{F}\{\mathcal{F}[s(t,G_y)]\}=[\mathcal{F}\{\mathcal{F}\{M_0\exp[i\phi(t,G_y)]\}\\ *_{f_x}\mathcal{F}[E_x(t)]*_{f_y}\mathcal{F}[E_y(G_y)]\\ *_{f_x}\mathcal{F}[d(t)]*_{f_y}\mathcal{F}[d(G_y)]]\\ \times\mathrm{III}(N_x\,\Delta t f_x)\mathrm{III}(N_y\,\Delta G f_y)\,,\end{aligned} \tag{8}$$

where $\mathcal{F}$ denotes the Fourier transform operator. The variables f_x and f_y correspond to t and G_y, respectively.

When the signal originates from a stationary point magnetization, represented by a delta function at (x_0, y_0), the phase given by Eq. (2) is particularly simple. In this case, the first factor in Eq. (8) is the following two-dimensional delta function:

$$\begin{aligned}&\mathcal{F}\{\mathcal{F}\{M_0\exp[i\phi(t,G_y)]\}\}\\ &\quad=M_0\,\delta[f_x-(\gamma/2\pi)G_x\,x_0]\,\delta[f_y+(\gamma/2\pi)t_y\,y_0]\,.\end{aligned} \tag{9}$$

In this work, the specific form of $E_x(t)$ is a decaying exponential. Consequently, $\mathcal{F}[E_x(t)]$ is the familiar Lorentzian. There is no apodization in the G_y direction and $\mathcal{F}[E_y(G_y)]$ is a delta function at the origin. Equation (10) represents the Fourier transform of Eq. (4); an equivalent expression applies for $\mathcal{F}[d(G_y)]$.

$$\begin{aligned}\mathcal{F}\{d(t)\}=N_x^2(\Delta t)^3\,\mathrm{III}(\Delta t f_x)\\ *_{f_x}\mathrm{sinc}(N_x\,\Delta t f_x)\,,\end{aligned} \tag{10}$$

where

$$\mathrm{sinc}(N_x\,\Delta t f_x)=\frac{\sin(\pi N_x\,\Delta t f_x)}{\pi N_x\,\Delta t f_x}\,. \tag{11}$$

The dimensions of f_x are reciprocal time, but those of f_y are m/T. In both cases, however, there is a direct relation to position,

$$f_x=(\gamma/2\pi)G_x\,x\,, \tag{12}$$

$$f_y=-(\gamma/2\pi)t_y\,y\,. \tag{13}$$

The phase inversion caused by the spin echo accounts for the negative sign in Eq. (13). The transformations to spatial coordinates, represented in Eqs. (12) and (13), are applied to the Fourier transformed signal, which is Eq. (8), to provide the point spread function,

$$\begin{aligned}\mathrm{PSF}(x,y)=K\,[P(x,y)*_x\mathcal{F}\{E_x(t)\}*_y\\ \cdot\mathcal{F}\{E_y(G_y)\}*_x D(x)*_y D(y)]\\ \cdot\mathrm{III}[N_x\,\Delta t(\gamma/2\pi)G_x\,x]\\ \cdot\mathrm{III}[N_y\,t_y\,\Delta G(\gamma/2\pi)\,y]\,,\end{aligned} \tag{14}$$

where

$$P(x,y)=M_0\,\delta(x-x_0)\delta(y-y_0)\,, \tag{15}$$

$$\begin{aligned}D(x)=\mathrm{III}[\Delta t(\gamma/2\pi)G_x\,x]\\ *_x\mathrm{sinc}[N_x\,\Delta t(\gamma/2\pi)G_x\,x]\,,\end{aligned} \tag{16}$$

and

$$\begin{aligned}D(y)=\mathrm{III}[\Delta G(\gamma/2\pi)\,t_y\,y]\\ *_y\mathrm{sinc}[N_y\,t_y\,\Delta G(\gamma/2\pi)\,y]\,.\end{aligned} \tag{17}$$

To simplify the presentation, arbitrary constants have been grouped into K. Of particular relevance is $P(x,y)$, defined in Eq. (15). Only this term in the PSF changes when a point moves. For this reason, derivations of the PSF of moving points are an extension of the previous development. With motion, Eq. (14) still applies, but $P(x,y)$ becomes more complicated than a delta function.

2. Motion

If movement alters the frequency of precession of a magnetization, it is unlikely to be assigned to the appropriate image point. In this case, the PSF less accurately represents the spin density. The simulations account for movement throughout the entire course of data acquisition. There can be significant cardiac motion within the typical 50-ms interval between excitation and the last data sample of one phase-encoded projection. During the same interval there is negligible displacement from breathing. Between sets of phase-encoded projections, however, sufficient time elapses for appreciable breathing motion to occur. Motion in each of the three orthogonal directions can be investigated separately for the following reason. Phase-sensitive detection separates the x and y positional dependence in the signal, as can be seen from Eqs. (2) and (3). Furthermore, the z coordinate does not affect the signal phase, but it determines the transverse magnetization, which is given by Eq. (1).

a. x motion. Motion in the x direction modulates the signal frequency because signals are measured under the presence of a magnetic field gradient in the x direction. Sinusoidal motion of amplitude A and frequency F along the x direction can be represented by Eq. (18). Time is represented by the variable T. The motion phase ϕ_x indicates the point in the cycle that corresponds to the zero of T,

$$x=x_0+A\sin(2\pi FT+\phi_x)\,. \tag{18}$$

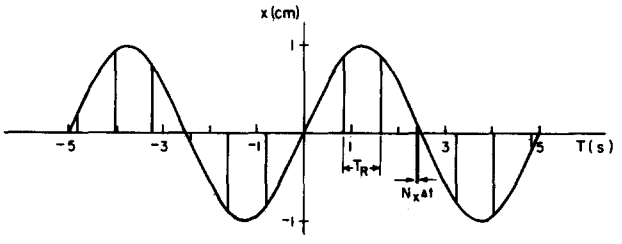

FIG. 4. Trajectory of a point in sinusoidal motion. Data sampling of duration $N_x\,\Delta t$ and repeated at intervals of T_R occurs at the positions shown. Since data sampling is periodic, T is readily expressed in terms of imaging variables. $x(T) = (1\text{ cm})\sin[2\pi(0.2\text{ Hz})T]$; $T_R = 0.8$ s; $N_x\,\Delta t = 15$ ms.

Figure 4 shows a point oscillating in the x direction and also indicates positions coincident with data sampling. Numerical values have been chosen to model breathing. It is apparent from this example that one phase-encoded projection is measured during a brief interval. To allow for relaxation, a comparatively long time T_R elapses between subsequent phase-encoded projections. Although data sampling can occur when the point is anywhere along its trajectory, positions near the displacement maxima are the most probable in sinusoidal motion.

Motion was incorporated into the PSF by substituting Eq. (18) into Eq. (2),

$$\phi(t,G_y) = \gamma\{G_x[x_0 + A\sin(2\pi FT + \phi_x)]\,t - G_y\,y_0\,t_y\}\,. \quad (19)$$

The duration of one signal is $N_x\,\Delta t$, and t is incremented discretely from $-[(N_x/2)-1]\Delta t$ to $(N_x/2)\Delta t$. Since a different phase-encoding gradient strength applies for each set of projections, T is related to G_y; G_y is stepped monotonically from $-[(N_y/2)-1]\Delta G$ to $(N_y/2)\Delta G$. We define the zero for T as the center of the echo of the signal which corresponds to a null phase-encoding gradient,

$$T = t + (G_y/\Delta G)T_R\,. \quad (20)$$

As previously stated, the effect of motion is introduced into the image only through the oscillatory part of the signal. The signal phase, which is expressed by Eq. (19), is separable into the variables t and G_y. Equation (22), which describes the phase of the signal under these conditions, follows from the identity[10] below:

$$\exp(ik\sin\theta) = \sum_{m=-\infty}^{\infty} \exp(im\theta)\,J_m(k)\,, \quad (21)$$

$$\exp[i\phi(t,G_y)] = \exp(i\gamma G_x\,x_0\,t)\exp(-i\gamma G_y\,y_0\,t_y) \cdot \sum_{m=-\infty}^{\infty} \exp(i2\pi mFt)\exp[i2\pi mF(G_y/\Delta G)\,T_R]\,\exp(im\phi_x)\,J_m(\gamma G_x\,At)\,. \quad (22)$$

Thus the continuous Fourier transform of the signal is given by

$$\mathcal{F}(\mathcal{F}\{M_0\exp[i\phi(t,G_y)]\}) = \left[M_0\,\delta\left(f_x - \frac{\gamma}{2\pi}G_x\,x_0\right)\delta\left(f_y + \frac{\gamma}{2\pi}t_y\,y_0\right)\right] *_{f_y} *_{f_x} \left[\sum_{m=-\infty}^{\infty} \exp(im\phi_x)\,(\delta(f_x - mF) *_{f_x} \mathcal{F}\{J_m(\gamma G_x\,At)\})\,\delta[f_y - (mFT_R/\Delta G)]\right]. \quad (23)$$

Equation (23) becomes clearer when expressed in terms of spatial coordinates. The final image is identical to that obtained for the stationary object, except for the $P(x,y)$ term,

$$P(x,y) = K\,[M_0\,\delta(x-x_0)\delta(y-y_0)] *_y *_x \left(\sum_{m=-\infty}^{\infty} \exp(im\phi_x)\left\{\delta\left(x - \frac{2\pi mF}{\gamma G_x}\right) *_x \mathcal{F}\,[J_m(\gamma G_x\,At)]\right\}\delta(y + my_G)\right), \quad (24)$$

$$y_G = \frac{2\pi FT_R}{\gamma\,\Delta G t_y}\,, \quad (25)$$

$$\mathcal{F}\,[J_m(\gamma\,G_x\,At)] = \begin{cases} \dfrac{2(-i)^m\,T_m(x/A)}{\gamma G_x(A^2-x^2)^{1/2}} & |x|<A\,, \\ 0 & |x|>A\,. \end{cases} \quad (26)$$

K incorporates all constants, J_m represents the mth-order Bessel function of the first kind, and T_m depicts the mth-order Chebyshev polynomial.[11]

Equation (24) shows how motion in the x direction affects the PSF. If the displacement amplitude A is zero, then Eq. (22) comprises only one term and Eq. (24) reduces, as expected, to Eq. (15). Only the x component of the two-dimensional artifact depends on the motion phase ϕ_x. Equation (26) vanishes for x greater than A, and it also peaks near the ends of the displacement, as would be expected from the probability distribution of an oscillating point. It may be noted in this equation, which was obtained from a continuous Fourier transform, that the maximum amplitude of higher order terms does not appear to decrease. This will be clarified later. Nonzero-order Bessel functions of argument zero are zero. Then, by a property of the Fourier transform, the integral over x in Eq. (26) vanishes for nonzero m, and leads to the same value for m zero as for a stationary point. Image inten-

FIG. 5. Simulated image of a point oscillating sinusoidally in x. Blurring in the x direction extends over a range of 2.0 cm. A 28×28 cm x–y plane is displayed. There are ghosts separated by 2.0 cm in the y direction. Motion parameters: $F = 0.2$ Hz, $A = 1.0$ cm, $\phi_x = 0$. Relevant imaging parameters: $T_R = 0.35$ s, $\Delta G = 0.33$ μT/m, $t_y = 2.5$ ms. Under these conditions, the predicted separation y_G is also 2.0 cm.

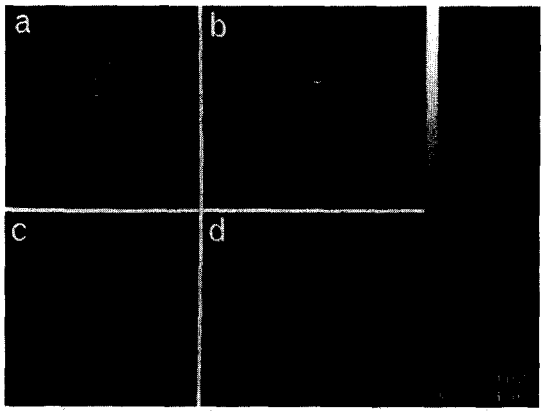

FIG. 6. Experimental images of an x–y plane with a small object oscillating sinusoidally along the x direction. Each quadrant is a separate image with a 28×28 cm field of view. Four images demonstrate how motion artifacts depend on the motion frequency F, amplitude A, and the repetition time T_R between signals (see Table I).

sity is therefore conserved. Convolution with the delta function in the x direction in Eq. (24) typically shifts each term described by Eq. (26) by less than 10 μm.

The last factor in Eq. (24) repeats the x-dependent line shape along the y direction. The spacing y_G is determined by Eq. (25). First, the higher the frequency of motion, the wider the spacing. Second, the longer the duration between changes in the phase encoding, the further apart are the repetitions. Third, decreasing either the duration or the amount by which the phase-encoding gradient is incremented increases the separation.

The previous theory accounts for many features in both simulated and experimental images. Figure 5 is a simulated image in the x–y plane for a point following Eq. (18). Although image intensities are complex numbers, the modulus is displayed. The image, then, is not a complete point spread function. Numerical values of the parameters were comparable to those employed in imaging. Although movement was confined to the x direction, the image contains bands spaced at constant intervals in the y direction. Equation (25) accounts for the separation of the bands. The brightest band is the blurred image of the point as it moves along x and, for this reason, it is not considered artifactual. The other bands are ghost artifacts.

The ghosts in the simulation extend far beyond the bandwidth, determined by sampling, and thus the image exhibits aliasing. Pixels with the greatest magnitude are bounded by the two limits of displacement. It appears that the artifact also extends beyond the boundary, but pixels have exceedingly small magnitudes. The image intensity within higher order ghosts slowly decreases. Equations (24) and (26), based on a continuous Fourier transform, however, do not predict this decrease. These last two equations are only part of the discrete PSF [Eq. (14)]. The convolutions in Eq. (14) decrease the amplitude of higher order ghosts especially, because these ghosts exhibit sharper peaks. Also, the variable t has a small range. With the parameters chosen, the argument of the Bessel function in Eq. (22) remains small, so that only a restricted portion of Eq. (22) is represented.

The theory also helps explain the four experimental MR images in Fig. 6. Each displays the modulus of the pixels in an x–y plane and results from a separate experiment. Relevant parameters and measurements are summarized in Table I. As alluded to previously, each phase-encoded projection was averaged four times before changing the amplitude

TABLE I. Summary of parameters and measurements of Figs. 6–8.

Figure	F (Hz)	A (cm)	T_R (s)	Spacing[a] (cm) p	m	Intensity relative to center (%) ghost	Simul. 1	Simul. 2	Exper. 1	Exper. 2
6(a)	0.1	1.0	0.8	2.3	2.1		65	60	75	60
6(b)	0.1	0.5	0.8	2.3	2.3		60	50	70	55
6(c)	0.2	1.0	0.8	4.6	4.3		65	55	80	60
6(d)	0.1	1.0	1.6	4.6	4.3		65	55	75	65
7(b)	0.2	0.25	0.8	4.6	4.7		65	50	70	50
7(c)	0.2	0.5	0.8	4.6	4.5		75	65	80	55
7(d)	0.1	0.5	0.8	2.3	2.3		75	60	80	60
8(a)	0.1	1.0	0.8	2.3	2.3		...	...	55	40
8(b)	0.1	2.0	0.8	2.3	2.2		...	...	55	55
8(c)	0.2	2.0	0.8	4.6	4.6		...	...	60	55
8(d)	0.1	2.0	0.8	2.3	2.3		...	...	75	50

[a] Values are for p (predicted) and m (measured) spacing.

of the phase-encoding gradient. As a result, four spatial positions of the point became associated with each phase-encoded projection. The experimental images, nevertheless, were analyzed with the theory previously developed. The repetition times in Table I, which were four times larger than in the actual experiments, were employed in the analytical expressions.

The experimental images, like the simulation, exhibit horizontal blurring and also uniformly spaced bands in the vertical direction. The displacement amplitude in Fig. 6(b) was one-half that of Fig. 6(a), and this halved the horizontal extent of the artifact, but left the spacing of the bands unchanged. The frequency of motion in Fig. 6(c) was twice that of Fig. 6(a), and the time between successive phase-encoded projections in Fig. 6(d) was doubled. As predicted by Eq. (24), the vertical separation of the ghosts also doubled. Bands which would have appeared outside the imaging field were "wrapped around" due to aliasing. The result is an apparent doublet structure.

The magnitude of the pixels within the ghosts decreased slowly with distance from the center of oscillation. For a quantitative appraisal, the magnitudes of pixels in regions comprising ghosts were summed. The sum was expressed as a percentage of the sum of the intensity of the band through the center of oscillation. The artifact pattern was symmetric about the center, as predicted, and ghosts on either side of the center were averaged. Table I summarizes the measurements on the experimental images in Fig. 6 and on simulations of the experiments. Averaging of the phase-encoded projections, in particular, was incorporated in the simulations. Intensity measurements on the experiments were systematically greater than on the simulations. The accuracy was estimated to be 10%. A major source of uncertainty was the overlap of ghosts, which was caused by aliasing. Measurements on the experimental images were compensated for background noise. Within the limits of accuracy, the intensity in each ghost was comparable in Figs. 6(a), 6(b), and 6(d). As expected, neither the frequency of oscillation, nor the repetition time, influenced the intensity. The intensity of the ghosts decreased with distance from the center. Furthermore, the decreased intensity within the ghosts in Fig. 6(b) was attributed to the smaller motion amplitude.

b. y motion. Displacement along the y direction disrupts the phase encoding by causing additional phase modulation of each signal. The duration of the y gradient is of the order of milliseconds—too short for breathing motion to be significant while the gradient is on. Since displacement perpendicular to the imaging gradient G_x does not affect the x component of the image, artifacts from movement in the phase-encoding direction arise from relocation of a magnetization between the application of successive y gradients. Figure 3 shows that motion along the y direction does not affect data sampling in a particular phase-encoded projection. Consequently, the motion time T depends only on G_y,

$$T = (G_y/\Delta G)T_R \,. \tag{27}$$

As with x motion, the data is separable in t and G_y, and motion changes only the $P(x,y)$ factor of the PSF for the point at rest,

$$P(x,y) = KM_0\,\delta(x-x_0)\,\delta(y-y_0) *_y \left[\sum_{m=-\infty}^{\infty} \exp(-im\phi_y)\,\delta(y-my_G) *_y (-1)^m \mathcal{F}\{J_m(\gamma A t_y G_y)\} \right]. \tag{28}$$

Constants are included in K, and y_G is the spacing of the artifact, which is given by Eq. (25). The artifact described by Eq. (28) is strikingly similar to that given by Eq. (24). The Fourier transform of the Bessel function is given by Eq. (26). The factor $(-1)^m$ arises from the transformation of Eq. (13). Equation (28) predicts that the point is blurred between the extremities of its displacement, this time in the y direction. A banding pattern is repeated along the phase-encoding direction at intervals of y_G. In this case, the structure of each band reflects the corresponding Chebyshev polynomial. The motion phase ϕ_y influences the artifact by modulating the distribution between the real and imaginary components of the image. The integral over y vanishes for each nonzero m term of Eq. (28).

Figure 7 contains images in an x–y plane from four experiments with sinusoidal motion of a small object in the y direction. The modulus of the complex image is displayed. As in all of the experiments, four phase-encoded projections were averaged before changing the strength of the phase-encoding gradient. Figure 7(a) is an image of the stationary point and identifies the center about which oscillations occurred. Images involving motion contained not only this central location, but also ghosts in the y direction. Table I reveals that the motion amplitude for Fig. 7(b) was one-half that in the two lower images, and as a result, blurring was less extensive. As expected, ghosts were closer together in Fig. 7(d), because the frequency of oscillation was reduced by a factor of 2.

As with x motion, quantitative analysis of the detailed structure of the experimental images was hampered by the overlap of ghosts. Averaging also limited the application of the theory. There was less image intensity in bands removed from the center of oscillation. The explanation that applied to x motion extends to this case. The intensity of several ghosts was determined in the same manner as before, and

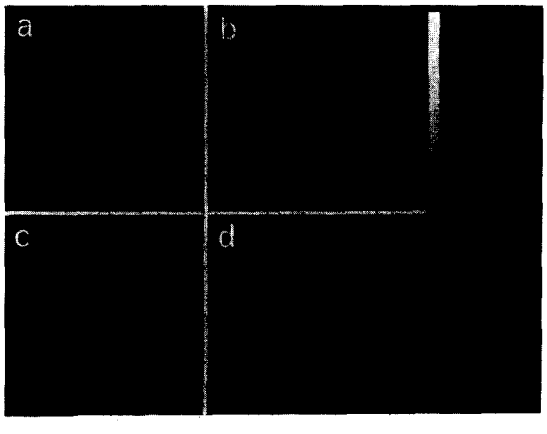

FIG. 7. Four experimental MR images of a 28 × 28 cm x–y plane. In (a) there was no motion, but in the remaining three images, the small object oscillated vertically about the position in (a) (see Table I).

summarized in Table I. There was close agreement between simulations and experiments. There was less intensity within the first two ghosts for the smaller amplitude motion. Furthermore, similar intensities in Figs. 7(c) and 7(d) support the theoretical prediction that the frequency of motion should not influence the intensity.

c. z motion. In most cases, there is insignificant movement during the selective excitation pulse, which lasts only a few milliseconds. The extent to which a magnetization is flipped depends essentially on the z coordinate at the start of excitation. An artifact will ensue if, for different signals, motion causes the transverse magnetization to differ in magnitude. Displacement perpendicular to the selected slice modulates the magnitude of the transverse magnetization. Then, M of Eq. (1) becomes a function of T, which is related to G_y through Eq. (27). Although signal phase is unaffected by z motion, the $P(x,y)$ factor of the PSF now incorporates the G_y dependence in M.

$$P(x,y,z) = KM_0 \exp\left[-\tfrac{1}{2}(\sigma\gamma G_z A)^2\right]\delta(x-x_0)\delta(y-y_0)$$
$$*_y \left\{\exp\left[-i\phi_z\,(y/y_G)\right] \sum_{m=-\infty}^{\infty} (i)^m I_m(\sigma^2\gamma^2 G_z^2 A z_0)\delta(y+my_G)\right\}$$
$$*_y \left\{\exp\left[-i\left(\phi_z - \frac{\pi}{4}\right)\frac{y}{y_G}\right] \sum_{n=-\infty}^{\infty} (i)^n I_n\left[(\tfrac{1}{2}\sigma\gamma G_z A)^2\right]\delta(y+n2y_G)\right\}. \quad (29)$$

I_m represents a modified Bessel function of the mth order, and all constants are incorporated in K.

Equation (29) predicts repetition at intervals y_G along the phase-encoding direction. Furthermore, the motion phase ϕ_z does not affect the magnitude of the artifact, but only influences the relative weight between the real and imaginary components of Eq. (29). What is unique to z motion is that the artifact becomes more complicated when the center of oscillation does not coincide with the center of the slice, but is a distance z_0 from the slice center.

The artifact from z motion depends on the shape of the selected slice, which was Gaussian, for the derivation. In this case, the relative magnitude of each term within the summation depends on the amplitude of motion. Simulations verified that higher order terms in the summation become significant for larger amplitudes. The dependence of the artifact on both the shape of the slice and the center of oscillation rendered simulation of the exact experimental conditions impractical.

Figure 8 presents four experimental images involving an object oscillating in the z direction. The center of oscillation did not coincide with the center of the slice, which was not Gaussian. As before, four phase-encoded projections were averaged. The modulus of the complex image is displayed in the selected x–y plane. As expected from Eq. (29), the artifact was confined to the phase-encoding direction. The intensity within the first two ghosts is summarized in Table I. Measurements on simulations could not be compared. Ghost artifacts are more apparent in Fig. 8(a) than in Fig. 8(b); there was less intensity in the first two ghosts for the motion with the smaller amplitude. The frequency of motion, not the amplitude, influenced the spacing of the ghosts. In particular, doubling the frequency of motion between Figs. 8(b) and 8(c) doubled the spacing. Aliasing caused ghosts to overlap in Fig. 8(c). The difference in Figs. 8(b) and 8(d) was the center of oscillation. Ghosts in both images are similarly spaced, but have different intensities relative to the center. This feature, too, is in agreement with Eq. (29).

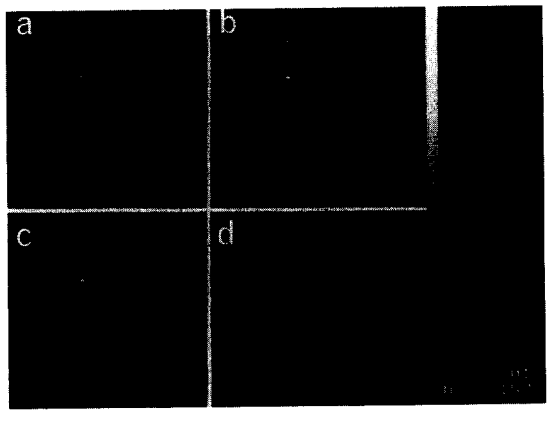

FIG. 8. Experimental MR images of a 28×28 cm x–y plane demonstrate the effects of oscillation perpendicular to the plane. Bands exhibit slight blurring in x due to vibration of the sample (see Table I).

B. Three-dimensional MR images

1. No motion

Artifacts from periodic motion in three-dimensional volume images differ from those in two-dimensional images. The technique to generate a three-dimensional image resembles that for two dimensions, except for the involvement of the z gradient. Immediately following a nonselective $\pi/2$ rf pulse, G_z is applied for t_z to phase-encode the z direction analogously to the y direction. The pulse sequence, which is a slight modification to Fig. 3, is repeated after delays of T_R, for all possible phase-encoding combinations. Data acquisition takes substantially longer than for a single two-dimensional slice. Specifically, for each G_z, there are N_y repetitions for each value of G_y. Then, the amplitude of G_z is altered for another N_y repetitions and this process is repeated N_z times to complete data acquisition. The mathematical representation of the complete data set is a straightforward extension of the two-dimensional case;

$$\phi(t,G_y,G_z) = \gamma(G_x\,xt - G_y\,yt_y - G_z\,zt_z), \quad (30)$$
$$s(t,G_y,G_z) = \{M_0 E_x(t)E_y(G_y)E_z(G_z) \cdot \exp[i\phi(t,G_y,G_z)]\, d(t)d(G_y)d(G_z)\}$$

$$*_t \text{ III}\left(\frac{t}{N_x \Delta t}\right) *_{G_y} \text{III}\left(\frac{G_y}{N_y \Delta G}\right) *_{G_z} \text{III}\left(\frac{G_z}{N_z \Delta G}\right), \tag{31}$$

where $d(G_z)$, the logical extension to the third dimension, retains the form of Eq. (5), and $E_z(G_z)$ describes apodization. Due to the separability of Eq. (31), and the similarity in the G_y and G_z dependence, three-dimensional PSFs resemble the two-dimensional PSFs previously derived. Three-dimensional Fourier transformation of the data, followed by conversion to spatial coordinates through Eqs. (12), (13), and (32), leads to the PSF, for

$$f_z = -(\gamma/2\pi) t_z z, \tag{32}$$

$$\begin{aligned}\text{PSF}(x,y,z) &= K\,[P(x,y,z) *_x \mathcal{F}\{E_x\} *_y \mathcal{F}\{E_y\} *_z \mathcal{F}\{E_z\} \\ &\quad *_x D(x) *_y D(y) *_z D(z)] \cdot \text{III}[N_x \Delta t (\gamma/2\pi) G_x x] \\ &\quad \cdot \text{III}[N_y t_y \Delta G (\gamma/2\pi) y] \text{III}[N_z t_z \Delta G (\gamma/2\pi) z]\,. \end{aligned} \tag{33}$$

K includes all constants. Apodization can be included by E_x, E_y, and E_z; there is no apodization in the y or z directions in the experiments. $D(x)$, $D(y)$, and $D(z)$ arise from the discrete nature of data sampling, and $D(x)$ is defined in Eq. (16). The simplest example is a stationary point object at (x_0, y_0, z_0). In this case, $P(x,y,z)$ is given by Eq. (34),

$$P(x,y,z) = M_0\, \delta(x - x_0)\delta(y - y_0)\delta(z - z_0)\,. \tag{34}$$

2. Motion

Even with motion, evaluation of the PSF proceeds as before, and the phase, which is given by Eq. (30), remains separable in t, G_y, and G_z. Since the z gradient now phase encodes analogously to the y gradient, motion introduces periodicity also in the z direction; since more time elapses between changes to the z gradient, the repeat distance along the z direction is substantially larger.

Sinusoidal motion in the x direction is still represented by Eq. (19). The motion time T is related to the imaging parameters through Eq. (35). After substituting the trajectory into the signal phase, $P(x,y,z)$ is evaluated,

$$T = t + (G_y/\Delta G) T_R + (G_z/\Delta G) N_y T_R\,, \tag{35}$$

$$\begin{aligned}P(x,y,z) &= K\,[M_0\, \delta(x - x_0)\delta(y - y_0)\delta(z - z_0)] *_z *_y *_x \\ &\cdot \left[\sum_{m=-\infty}^{\infty} \exp(im\phi_x) \cdot \left(\delta\left(x - \frac{2\pi m F}{\gamma G_x}\right)\right.\right. \\ &\left.\left. *_x \mathcal{F}\{J_m(\gamma G_x A t)\}\right) \delta(y - m y_G)\delta(z - m N_y y_G)\right]. \end{aligned} \tag{36}$$

The last factor of Eq. (36) propagates bands along the z direction; their separation is N_y times greater than the repetitions in the y direction, and they would extend beyond the image volume if aliasing did not fold them back.

Motion along the z direction in three-dimensional imaging does not alter the transverse magnetization, but is completely analogous to y motion. Instead, both y- and z-directed motion disrupt the regular phase encoding in the same way. The motion time T no longer depends on the data sampling time t. Because of the similarity between phase encoding in the y and z directions, $P(x,y,z)$ for the case of y motion only is presented,

$$\begin{aligned}P(x,y,z) &= K\,[M_0\, \delta(x - x_0)\delta(y - y_0)\delta(z - z_0)] *_z *_y \\ &\times \left(\sum_{m=-\infty}^{\infty} \exp(-im\phi_y)(-1)^m \right. \\ &\left. \times \{\mathcal{F}[J_m(\gamma A t_y G_y)] *_y \delta(y - m y_G)\}\, \delta(z - m N_y y_G)\right). \end{aligned} \tag{37}$$

Since motion artifacts in three-dimensional imaging are not confined to a plane, their illustration is more complicated. In Fig. 9, planes with y and z orientations from four different three-dimensional images were selected. As well as blurring along the direction of motion, in all cases there are ghosts in both phase-encoding directions. Note that even the first ghost of all of the images was aliased in the z direction. During the acquisition of the upper images there was oscillation only along the z direction; the motion frequency in the upper left image was twice that in the upper right image. There are bands repeated not only along the y direction (vertical), but also in the z direction (horizontal). The separation in both directions is greater for the higher frequency motion. As expected, within one ghost the intensity is greatest at both ends of displacement. Similarly, Fig. 9(c) typifies images involving oscillation in the y direction. As expected, the point is blurred vertically. Finally, Fig. 9(d) demonstrates horizontal sinusoidal motion. Here the artifact and image are not confined to a single x coordinate and, therefore, only some of the artifact is revealed in this y–z plane.

IV. SUMMARY

The point spread function has been calculated for both a stationary point object and one executing simple harmonic motion. Through comparison with experimental images, two effects of motion have been identified. First, there is blurring between the limits of displacement. Second, a coherence develops between the imaging steps and the motion, which is expressed as ghost structures repeated along the

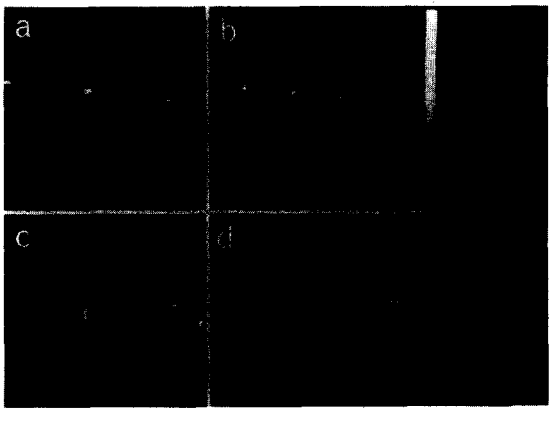

FIG. 9. The same 28×28 cm y–z plane (y vertical, z horizontal) from four different three-dimensional images. For all of the experiments, the repetition time was 0.2 s and the displacement amplitude was 0.5 cm. Direction of motion and motion frequency F in Hz: (a) z, 0.2; (b) z, 0.1; (c) y, 0.2; and (d) x, 0.2.

phase-encoding direction(s). Although consecutive data samples are separated by microseconds, the time interval between signals with changed phase encoding is in the range of seconds. In three-dimensional images, a much longer time passes before a change to phase encoding in the z direction. Consequently, spacing between ghosts is too small to discern in the x direction, on the order of centimeters in the y direction and, in three-dimensional imaging, sufficiently large to be completely aliased in the z direction. In three-dimensional images, motion artifacts are not confined to individual slices, and motion anywhere within the imaging volume can affect the entire image. It might, therefore, be preferable to acquire separate images of consecutive slices, instead of an entire volume, and thereby confine the extent of motion artifacts.

The point spread function analysis has led to a quantitative characterization of motion artifacts. Although one specific imaging technique was considered, some results are general. The most apparent feature of the artifact, the spacing between ghosts, arose from the long time interval between successive phase-encoded projections. Other imaging techniques which employ phase encoding and require long imaging times would also exhibit ghosts. Finer structure of motion artifacts, however, would depend on the particular technique. It should be possible to eliminate motion artifacts if the trajectory of the motion is completely known. It remains to be determined, however, how much prior knowledge of the motion is necessary, and also whether proposed corrections can be implemented in practice.

ACKNOWLEDGMENTS

This investigation was supported by the Ministry of Health of the Province of Ontario, the National Cancer Institute of Canada, and the Ontario Cancer Treatment and Research Foundation. One of the authors (MW) is a recipient of the Harold E. Johns Fellowship in Medical Physics.

[1]G. Harauz and M. J. Bronskill, J. Nucl. Med. **20**, 733 (1979).
[2]R. L. Dixon and K. E. Ekstrand, Med. Phys. **9**, 807 (1982).
[3]*Program and Book of Abstracts*: *The Society of Magnetic Resonance in Medicine* (Society of Magnetic Resonance in Medicine Inc., Berkeley, 1983).
[4]P. Mansfield and P. G. Morris, *NMR Imaging in Biomedicine* (Academic, New York, 1982).
[5]A. Kumar, D. Welti, and R. Ernst, J. Magn. Reson. **18**, 69 (1975).
[6]W. S. Hinshaw and A. H. Lent, Proc. IEEE **71**, 338 (1983).
[7]W. A. Edelstein, J. M. S. Hutchison, G. Johnson, and T. Redpath, Phys. Med. Biol. **25**, 751 (1980).
[8]R. N. Bracewell, *The Fourier Transform and its Applications*, 2nd ed. (McGraw–Hill, Toronto, 1978), p. 78.
[9]Reference 8, p. 52.
[10]*Handbook of Mathematical Functions*, edited by M. Abramowitz and I. A. Stegun, National Bureau of Standards Applied Mathematics Series 55 [Natl. Bur. Stand. (U.S.), Washington, D.C., 1964], p. 361.
[11]Reference 10, p. 486.
[12]M. Haacke, Picker International (personal communication).